Magnetic Resonance Imaging in Situ Visualization of an Electrochemical Reaction under Forced Hydrodynamic Conditions

María Raquel Serial,[†,‡] Manuel Isaac Velasco,[†,‡] Santiago Agustín Maldonado Ochoa,[†,‡] Franco Martín Zanotto,[§,∥] Sergio Alberto Dassie,[§,∥] and Rodolfo Hector Acosta*[,†,‡]

[†]Facultad de Matemática, Física, Astronomía y Computación, Universidad Nacional de Córdoba, Medina Allende s/n, X5000HUA Córdoba, Argentina
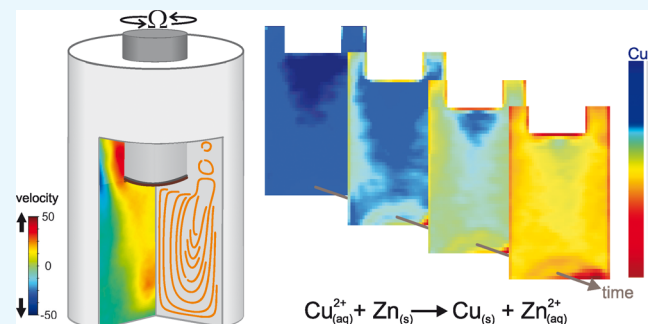
[‡]Instituto de Física Enrique Gaviola (IFEG), CONICET, Medina Allende s/n, X5000HUA, Córdoba, Argentina

[§]Departamento de Fisicoquímica, Facultad de Ciencias Químicas, Universidad Nacional de Córdoba, Ciudad Universitaria, X5000HUA, Córdoba, Argentina

[∥]Instituto de Investigaciones en Fisicoquímica de Córdoba (INFIQC), CONICET, Ciudad Universitaria, X5000HUA, Córdoba, Argentina

S *Supporting Information*

ABSTRACT: Magnetic resonance imaging (MRI) has proven to be a powerful tool for the characterization and investigation of in situ chemical reactions. This is more relevant when dealing with complex systems, where the spatial distribution of the species, partition equilibrium, flow patterns, among other factors have a determining effect over mass transport and therefore over the reaction rate. The advantage of MRI is that it provides spatial information in a noninvasive way and does not require any molecular sensor or sample extraction. In this work, MRI is used to fully characterize an electrochemical reaction under forced hydrodynamic conditions. Reaction rates, flow patterns, and quantitative concentration of the chemical species involved are spatially monitored in situ in a complex system that involves metallic pieces and a heterogeneous cementation reaction. Experimental data are compared with numerical simulations.

$$Cu^{2+}_{(aq)} + Zn_{(s)} \longrightarrow Cu_{(s)} + Zn^{2+}_{(aq)}$$

INTRODUCTION

Understanding the course of electrochemical reactions involves an in-depth study not only of the electron transfer events that take place but also of the vast number of factors that affect that process. In complex systems, the spatial distribution of the species, partition equilibrium, flow patterns, among others have a determining effect over mass transport, therefore over the reaction rate. Magnetic resonance imaging (MRI) has proven to be a noninvasive, powerful, and versatile tool to monitor a wide variety of chemical processes.[1−3] In the last few years, several studies have used MRI to monitor chemical processes in situ, leveraging its ability to provide spatial information about the system.[4−7]

However, monitoring electrochemical reactions brings up several technical obstacles that need to be overcome. The most evident is the presence of metallic pieces, such as electrodes, in the interior of the magnet; resulting in magnetic field inhomogeneities in the vicinity of the metal. These inhomogeneities interfere with the well-defined linear magnetic field gradients, which are used for spatial encoding during MRI, and this essentially leads to distortions in the final image. It has been shown that these image defects can be minimized by aligning the metallic parts of the electrochemical cell parallel to the static magnetic (B_0) field of the magnetic resonance imager and the RF (B_1) field, that is, lying in the plane defined by both fields.[8] However, it is not always possible to modify the cell design without affecting its performance.

Image artifacts are also dependent on the pulse sequence employed, where spin echo-based sequences have shown to be more robust in medical applications when metal parts are involved.[9,10] However, the minimum acquisition time using this pulse sequence is around a few minutes. There are other pulse sequences that allow obtaining images in less than 1 s, for instance, rapid acquisition relaxation (RARE) and echo planar imaging (EPI) sequences are among the best known.[11−13] Yet, configurations based on a gradient echo such as the EPI sequence are very sensitive to the presence of metallic structures, whereas the sequences based on a spin echo, such as the spin eco and RARE, apply refocusing pulses that correct the field inhomogeneity throughout the sample. The RARE sequence was recently used to provide insights into mass transfer processes in a chemical reaction by MRI in real time,

where freely diffusing ions in solution were mapped during the electro-dissolution of copper.[14] Although there is a vast amount of systems where species transport occurs only by diffusion, in several technological applications, mass transport is enhanced by mixing, stirring, or kneading. The implementation of this technique under the presence of flow requires that the excited volume does not move significantly during the acquisition of the image, which limits the application of this sequence to several systems where high velocities or nonideal flow patterns are present. This is the main reason why, to the best of our knowledge, MRI has been so far used to monitor electrochemical reactions where only diffusive mass transport was present and in constant motion throughout the acquisition time.

We have proved that velocity MRI is a useful tool to characterize the velocity profiles that take place in the interior of a rotating disk electrode (RDE) cell.[15−17] Electrochemical cells with a RDE configuration are widely used to characterize electrochemical reactions.[18−20] It can be used to measure the stoichiometric number of electron transfer in the electrochemical reaction, bulk concentration and diffusion coefficient, reaction kinetic constant and reaction intermediates in studying electrode reaction kinetics and mechanisms. RDE is easy to construct with a variety of electrode materials, and it is amenable to rigorous theoretical treatment. The former attribute makes it interesting for its study with computational methods.[21] In this setup, mass transfer and the associated velocity profiles near the electrode play a main role in the analysis of the information obtained. The spinning disk drags the fluid at its surface along with it and, because of centrifugal force, flings the solution outward from the center in a radial direction. The fluid at the disk surface is replenished by a flow normal to the surface. Our previous studies were made to fully understand the mass transport processes that take place under forced hydrodynamic conditions. The aim of this paper is to use MRI to monitor a chemical reaction under forced hydrodynamic conditions, where a convective flow pattern is generated and metallic parts are present. As a model reaction, we chose the cementation of copper over a zinc plate, not only for its simplicity but also due to its high impact over hydrometallurgical process. Cementation is one of the oldest hydrometallurgical techniques, and it is applied in wide variety of industrial areas or effluent treatments.[22−25] In general, this is a single displacement reaction that involves a reductive precipitation of a metal ion from a solution through a series of galvanic reactions, in which electrons are transferred from the less noble metal through the growing metallic deposit. Because during the reaction, a solid deposit is formed, this implies that the geometry of the system is modified and so could be the mass transport patterns in the RDE cell. In this way, MRI is a promising tool that will allow us to monitor not only the reaction course but also the spatial codification of all of the species involved, as well as its flow pattern.

RESULTS AND DISCUSSION

Imaging Artifact Minimization. It is well-known that the impact of artifacts caused by metallic objects depends mainly on the relationship between the geometry of interest and the orientation of the object relative to the magnet's magnetic field (B_0) direction.[26] The main field strength plays a less important role, but its orientation depends on the type of imager. When dealing with metallic electrodes, the main cause of the artifacts is the difference in the magnetic susceptibility and Foucault

currents induced either when the gradient coils are turned on or by the radiofrequency field, B_1.

Because of differences in the magnetic susceptibility, local field inhomogeneities are generated, which give rise to several geometric distortions in the read direction, disturbances in the excited slice, and signal intensity variations. As expected, metals with higher magnetic susceptibilities produce bigger defects in the image. Therefore, nonmetallic electrodes or zinc and copper are the elements of choice in these applications.

The image distortions produced by a Zn plate were studied. The use of rectangular plates as electrodes for the study of electrochemical reactions has been previously studied,[5,27] where it was shown that the distortions are minimized when orienting the plates with the direction of the radiofrequency field B_1. However, in the RDE configuration, the electrode is placed on the base of an insulating material rod, which rotates at a given angular frequency. Emulating this arrangement, a Zn plate was placed on the base of the rod (see Figure 1a) in order
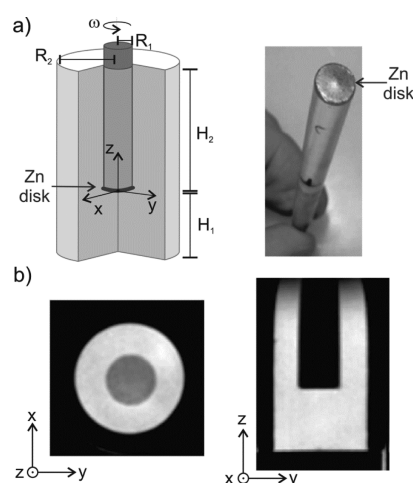

Figure 1. (a) Schematic representation of the RDE cell and photography showing the position of the Zn plate. (b) MRI of distilled water in the RDE with the Zn plate. Two slices are shown, a $x−y$ plane (left image) where a slice close to the rod is selected; and a $z−y$ plane (right image) in the center of the cell along the x direction. No significant image alterations are observed close to the metal.

to evaluate the image distortions produced in the system. In this configuration, the orientation of the disk is perpendicular to B_0, whereas the normal to the metal surface is perpendicular to B_1 (applied in the $x−y$ plane).

Images of the cell filled with distilled water are shown in Figure 1b. To monitor possible artifacts in several image directions, different planes were acquired using the pulse sequence described in the Supporting Information. On the left of Figure 1b, the $x−y$ plane of the cell is shown. For this purpose, a slice of 3 mm thickness was selected along the z direction and centered on the base of the rotating rod. On the other hand, a $z−y$ plane of 3 mm thickness along x is shown on the right. In both images, it is clearly observed that in this configuration, the presence of the zinc disk does not produce distortions in the image.

Relaxation Contrast. NMR provides several ways to monitor chemical reactions. Spectroscopy is one of the preferred techniques when determining the concentrations of reactants as the reactions proceed.[28−30] However, this is only possible when the chemical species involved in the electro-

chemical reaction have NMR active nuclei, such as ^{1}H, ^{7}Li, or ^{23}Na, among others.[31−33] With these nuclei, it is also possible to study complex systems by MRI.[7,27] Another strategy for the mapping of chemical reactions is through the determination of local changes in the systems relaxation rates. For instance, because of the electronic configuration d^9, Cu^{2+} cations are paramagnetic, so the relaxation the NMR signals of ^{1}H of water molecules in the solution is significantly modified. The ionic species involved in the studied redox reaction are described by chemical eq 1

$$Cu_{(aq)}^{2+} + Zn_{(s)} \rightarrow Cu_{(s)} + Zn_{(aq)}^{2+} \tag{1}$$
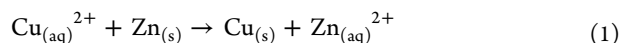
As the cementation reaction proceeds, the concentration of the paramagnetic cation decreases and the solvent molecule relaxation time increases.[34] If no other paramagnetic species are generated, the solution relaxation time T_1 can be used as a useful parameter to monitor the redox reaction. Figure 2 shows
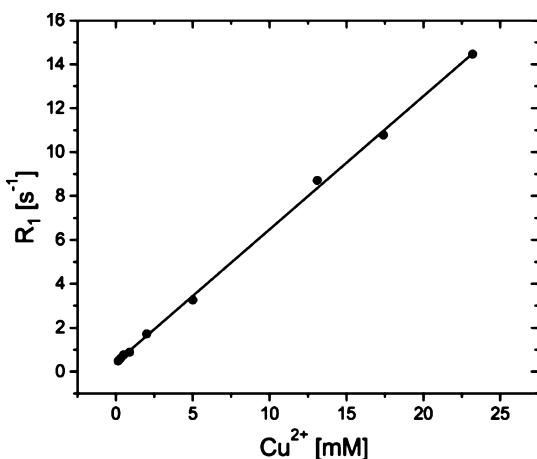

Figure 2. Relaxivity (R_1) as a function of the cupric ion concentration.

the linear dependency between [Cu^{2+}] and the relaxivity $R_1 = 1/T_1$ in solutions with concentrations ranging from 0 (pure water) to 25 mM CuSO$_4$. Because in the chemical reaction between Cu^{2+} and Zn, the generated Zn^{2+} is not paramagnetic and the linear fitting of the plot can be used to monitor the cementation evolution. The difference in the relaxation times can also be used as a contrast mechanism in MRI, where the signal intensity in an image pixel is proportional to the T_1 value and to the transverse relaxation time T_2 that accounts for the magnetization evolution during the imaging period (see the Supporting Information). This allows the monitoring of the spatial distribution of metal ions in the sample, as the cementation reaction proceeds.

Monitoring Chemical Reaction Evolution. As a first step, the overall chemical reaction kinetics is determined by changes in the relaxation time of the RDE cell as a whole. That is, MRI is not yet performed, whereas the signal corresponds to the whole cell. The reaction evolution under convective flow was monitored by means of changes in the relaxation times T_1. A rotating rod with a Zn plate attached at its base was immersed in a 25 mM CuSO$_4$ solution. Several rotation speeds were tested, ranging from 0 to 94.2 Hz. As the reaction proceeds, the relaxation time of the solvent increases reaching a final value of T_1 = 1.9 s, which is similar to that of the pure water, evidencing that the generated Zn^{2+} has a lesser effect over the solution T_1 value. Figure 3a shows how the global
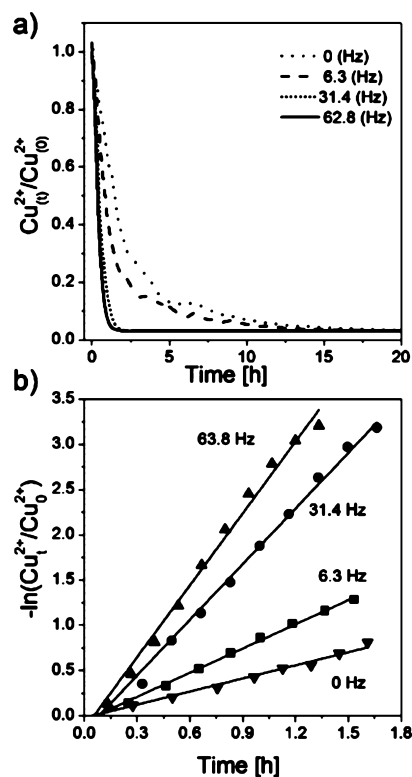

Figure 3. Reaction monitoring by means of the relaxation time T_1. (a) Cupric ion concentration variation at different rotation speeds and (b) same after the first-order linearization. k values are obtained from the linear fit of (b). Data obtained from the reaction at 94.2 Hz are not shown for clarity because it overlaps with data obtained at 62.8 Hz.

Cu^{2+} concentration decreases as the cementation process proceeds. It has been reported by several authors that cementation reactions follow first-order kinetics.[35−37] Thus, the following expression is valid

$$-\log\left(\frac{C_{Cu^{2+}}(t)}{C_0}\right) = kt \tag{2}$$

where k is a first-order rate constant, t is the time, C_0 is the initial Cu^{2+} concentration, and $C_{Cu^{2+}}(t)$ is the average Cu^{2+} concentration for the whole cell as a function of time. Figure 3b shows the first-order linearization of the data in Figure 3a according to eq 2.

As expected, the reaction rate increases with the rotational speed.[23,24,37−39] This can be attributed to a decrease in the diffusion layer thickness, which yields a more efficient Cu^{2+} transport rate from the solution bulk to the metal surface.

From the first-order plots, it is possible to determine the reaction rate constant by simply applying a linear fit. It can also be observed that for lower rotational speeds, the late stages of the cementation behavior deviate from first-order kinetics because of the prevalence of mass transport by diffusional control. The reaction rate values thus obtained are reported in Table 1, where it can be observed that the cementation rate increases as the rotational speed increases. However, a maximum value of 2.5 h^{-1} is reached at 62.8 Hz, and a further increase in the rotational speed does not substantially affect the reaction rate.

For the RDE configuration, the Levich equation describes the current response of mass transfer limited electrochemical

Table 1. First-Order Rate Constant k (from Experiment) and k_m (eq 3) Obtained at Different Rotational Speeds (Ω)

Ω/Hz	k/h^{-1}	k_m/10^{-6} m s^{-1}
0.0	0.51	diffusion limited
6.3	0.83	1.08
31.4	1.90	2.42
62.8	2.51	3.42
94.2	2.53	4.19

reactions.[19,40] This equation[41] that includes Cochran's approximate analytical solution[42] for the fluid velocities assumes that the depth of the cell and the rotating plane are infinite and the thickness of the electrode is negligible. The dimensions of the cell are considered infinitely large, thus avoiding the rebound of the fluid against the walls of the same. From it, an expression for the mass transfer coefficient k_m (in m s^{-1}) can be deduced[19]

$$k_m = 0.62\, D^{2/3} \nu^{-1/6} \Omega^{1/2} \tag{3}$$

where D is the diffusion coefficient of the reactant species and ν represents the kinematic viscosity of the solution. Additionally, as shown by multiple authors,[24,35,39,43,44] the first-order rate constant k (in s^{-1}) can be expressed in terms of k_m as

$$k = AV^{-1}k_m \tag{4}$$

where V is the solution volume and A is the effective area of the Zn plate. Thus

$$k = 0.62(AV^{-1})D^{2/3}\nu^{-1/6}\Omega^{1/2} \tag{5}$$

For the purposes of this work, AV^{-1} will be kept as an adjustable characteristic reciprocal length. Finite element method simulations were carried out in order to validate this dependence, and results are detailed in the electronic Supporting Information.

The first-order rate constant was calculated by averaging the concentration over the whole of the solution, linearizing, and fitting a linear function. In all cases, the fit was very satisfactory ($r^2 \geq 0.9999$), which corroborates that the reaction is first-order with respect to $C_{Cu^{2+}}$.

In order to validate eq 5, simulations were carried out for different rotational velocities, kinematic viscosities, and diffusion coefficients. Then, k was plotted as a function of the reduced parameter $\nu^{-1/6}D^{2/3}\Omega^{1/2}$ for different sets of kinematic viscosities, diffusion coefficients, and rotational speeds (Figure 4). As can be seen, the linear behavior of these plots validates the use of this equation for this system.

Additionally, useful parameters can be obtained from the computer simulation which are inaccessible in MRI experiments. For instance, a current can be defined, even if no external circuit is present. It can be interpreted as the amount of charge transferred per unit time between the Zn and Cu species. From the simulations, this current, i_L, can be obtained as

$$i_L = nF \int_0^{r_{Zn}} D \frac{\partial C_{Cu^{2+}}}{\partial z} r\, dr \tag{6}$$

where n is the number of exchanged electrons, F is the Faraday constant, and r_{Zn} is the Zn plate radius. The argument in this integral is the flux of Cu^{2+} ions toward the interface. This current can be compared with that predicted by the Levich equation
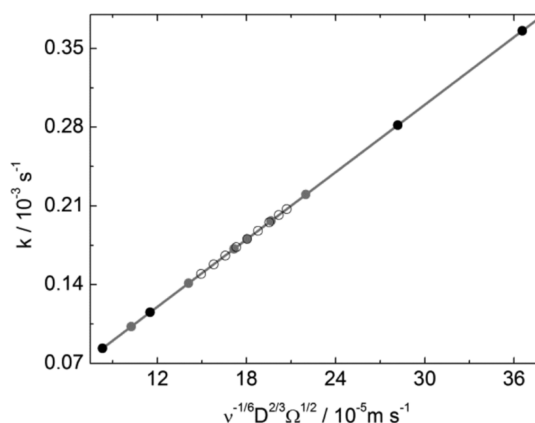
Figure 4. Simulation results used to validate the use of eq 5. Rate constant as a function of the reduced parameter $\nu^{-1/6}D^{2/3}\Omega^{1/2}$ and corresponding linear fit. Each of the three parameters was varied while keeping the other two constants. ν was varied from 3.3×10^{-7} to 3.8×10^{-6} m^2 s^{-1} (white circles). D was varied from 3×10^{-10} to 1.3×10^{-8} m^2 s^{-1} (black circles). Ω was varied from 6.3 to 94 Hz (gray circles). When constant, parameters were kept at: $D = 1 \times 10^{-9}$ m^2 s^{-1}, $\nu = 1.0097 \times 10^{-6}$ m^2 s^{-1}, and $\Omega = 62.8$ rad s^{-1}. Fitting parameters: $r^2 = 0.99989$, intercept = $\nu = 9.51 \times 10^{-6}$ s^{-1}, slope = 2.15 m^{-1}.

$$i_L(t) = k_m nFAC^*(t) \tag{7}$$

where A is the plate area and $C^*(t)$ is the average concentration in the cell; in this case, it is a function of time because the reactant is consumed as the reaction proceeds. The importance of this equation lies in that it links the interfacial processes to the average concentrations throughout the cell of cupric ion. Thus, k_m can be obtained from the slope of the plot of i_L as a function of average concentration and compared with its analytical expression (eq 3). A computer simulation was carried out matching the parameters with the experimental conditions ($\nu = 1.0097 \times 10^{-6}$ m^2 s^{-1}, $D = 0.583 \times 10^{-9}$ m^2 s^{-1}, $\Omega = 62.8$ Hz). For the determination of the mass transfer coefficient from eq 7, the current $i_L(t)$ was calculated by integrating the $C_{Cu^{2+}}$ flux perpendicular to the Zn plate in the revolved geometry and multiplying the result by nF. Figure 5 shows the plot of current as a function of average
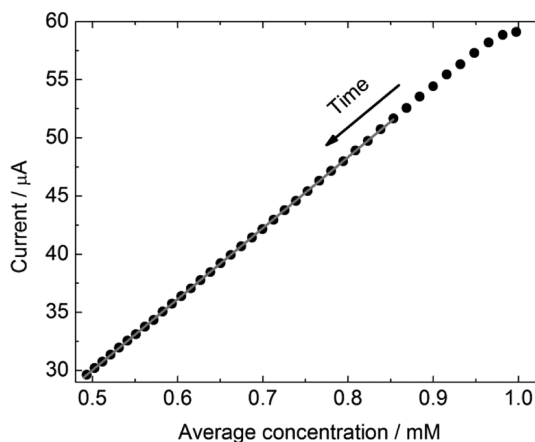
Figure 5. Current, according to eq 6, as a function of average concentration throughout the cell. The linearized slope corresponds to $k_m nF A$. Fitting parameters: $r^2 = 0.99997$, intercept: -5.0×10^{-7} A, slope: 6.11×10^{-6} A mM^{-1}.

concentration; for later simulation times, a straight line is obtained. After discarding the data corresponding to early stage, linear regression yields a k_m value of 1.12×10^{-5} m s^{-1}.

For these parameters, eq 3 yields a value of 1.08×10^{-5} m s^{-1}. This 3.7% mismatch can be attributed to the fact that the concentration is not completely homogeneous throughout the cell and that the Levich equation is not completely valid for small cells. The value of k was determined for these conditions to be 3.48×10^{-5} s^{-1}. From eq 4, AV^{-1}, the adjustable characteristic reciprocal length, was calculated to be 3.42 m^{-1}.

This good agreement confirms that k_m, as calculated from eq 3, is a valid parameter to characterize mass transport in systems involving cementation under forced hydrodynamic conditions. The corresponding values for the performed experiments are presented in Table 1.

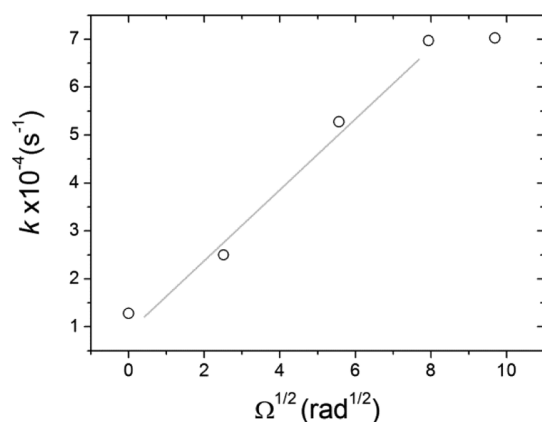Figure 6 shows the cementation rate constants as obtained from experiments plotted as a function of the square root of Ω.

Figure 6. Variations of rate constant (k) obtained for various rotation speeds (Ω) as a function of the square root of the disc rotation speed. The gray line is a guide to the eye.

It can be observed that the linear dependence is not maintained for rotational speeds higher than 62.8 Hz.

The deviation from the linear behavior at higher rotational speeds indicates that in these conditions, eq 5 is not valid. This could be attributed to two main causes: first, the assumption that mass transport is the limiting factor at such high rotational speeds might not be completely valid, as electron transfer becomes a limiting factor in the reaction rate. Second, we have previously shown by means of velocity MRI experiments that rotational speeds above 62 Hz lead to the formation of vortices and the fluid dynamics within this cell deviate from ideal behavior.[15,16] In particular, the velocity profile in the z direction shows that the velocity of the fluid going from the

bulk reservoir to the electrode surface increases with rotational speed, but the streamlines lose the homogeneous and parallel distribution because of the formation of vortices, as shown in Figure 7. It can be observed that at high rotational speeds, the material does not arrive to the metal surface in a homogeneous way, with faster dynamics in the borders of the rod and slower velocities in the center, in concordance with previous results.[45] Thus, reaction rates deviate from those predicted by eq 5 because it is formulated assuming an ideal fluid dynamics, considering laminar flow and velocities tangential to the metallic disc.

MRI Visualization of a Chemical Reaction. We now turn our attention to the determination of velocity profile information. Although the pulse sequence described in the previous section showed to be robust to the effects produced by metallic materials, the minimum acquisition time for an image is 1 min. Because the reaction rate increases with the frequency of rotation of the rod, it was decided to use a low rotation frequency for these MRI experiments, in order to be able to monitor all of the possible details in the acquired images. Several aspects must be considered in the pulse sequence implementation when dealing with the determination of flow with MRI. Whilst a detailed description of the pulse sequence is provided in the Supporting Information, here we mention the basic points to be considered. The basic idea is to determine changes in the phase of the NMR signal in a given section of space, namely, a voxel. It is important during the acquisition time that the monitored molecules do not move more than half the distance of the voxel. This imposes a maximum velocity to be encoded. On the other hand, codification is carried out by the application of a pair of bipolar magnetic field gradient pulses. The amplitude and duration of these pulses determine the so-called field of flow. The hardware limitation set for these parameters determines the accuracy in the determination of low velocities. It is clear that the particular flow patterns and hardware must be carefully tuned for an optimum acquisition. A thorough discussion for the particular setup used in this work may be found in ref 15. After choosing the proper parameters for image acquisition (see the Supporting Information for a further details), the cementation process was monitored every 90 s over a period of 1.3 h. Image intensities were transformed to Cu^{2+} concentration maps, as shown in Figure 8 for a series of representative reaction times.

The distribution of Cu^{2+} is not homogeneous through the volume of the cell. The higher concentrations are observed to be near the electrode surface, whereas a lower concentration is present in the recirculation areas. At $t = 3150$ s, solid copper that has been deposited at the bottom of the cell is observed.
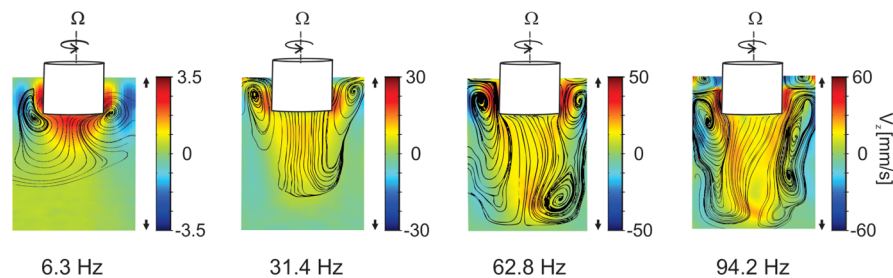

Figure 7. Velocity maps and streamlines of a RDE for different rotational speeds. Color plot shows the values of velocities in the z direction, whereas streamlines are built from the data of z and y velocities.
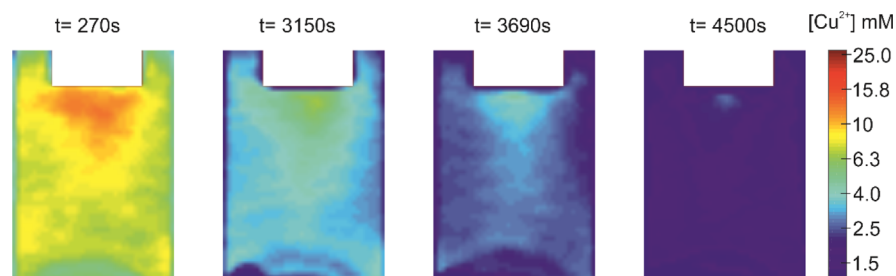
Figure 8. Cu^{2+} concentration maps at different reaction times.

Because the speeds in the lower part of the cell are minimal, the precipitated copper remains immobile during the experiments. As the reaction develops, the concentration of Cu^{2+} ions decreases in a large part of the volume of the solution. The combination of the velocity maps (Figure 7) and cupric ion concentration maps (Figure 8) obtained by MRI provides insight into the mass transport phenomena that takes place and the consequent chemical reaction. The streamlines denoted in Figure 7 show how liquid flows inside the cell. By comparing it with Figure 8, it can be seen that the solution that moves from the bottom of the cell to the electrode has a high Cu^{2+} concentration, whereas the borders and the vortices in the upper part have a lower concentration. MRI evidences how the paramagnetic ions travel from the bottom of the cell toward the electrode and then react to generate Zn^{2+} ions, which are expelled to the sides of the cell and mixed with the remaining Cu^{2+} solution. Then, the solution recirculates in a new cycle from the sides to the bottom and up to the Zn plate, until the reaction is over.

The distribution of reactant arising from the convective−diffusive mass transport can be interpreted more clearly from the concentration profiles at the center of the cell, extracted from the Cu^{2+} maps, which are shown in Figure 9. The
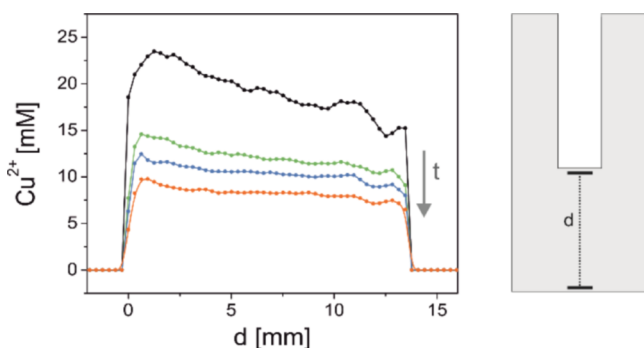

Figure 9. (Left) Cu^{2+} concentration profiles, taken from the center of the cell along the axial direction d, during the course of the reaction. The selected times are 270 s (black), 3150 s (green), 3690 s (blue), and 4500 s (orange). (right) Schematic representation of the electrochemical cell indicating the dimension d, where $d = 0$ corresponds to the Zn plate.

position $d = 0$ corresponds to the location of the Zn plate. The concentration profiles show a decrease in Cu^{2+} ions for $d = 0$. This behavior agrees with the work presented by Alexiadis et al.,[21] where a model reaction is simulated in an RDE cell under forced hydrodynamic conditions.

In order to monitor the distribution of the reactant species as a function of time, the concentrations associated with the immediate vicinity of the Zn plate ($d = 0.313$ mm) and for a

point at the center of the cell ($d = 7$ mm) as a function of time are shown in Figure 10a. For times lower than 540 s, the
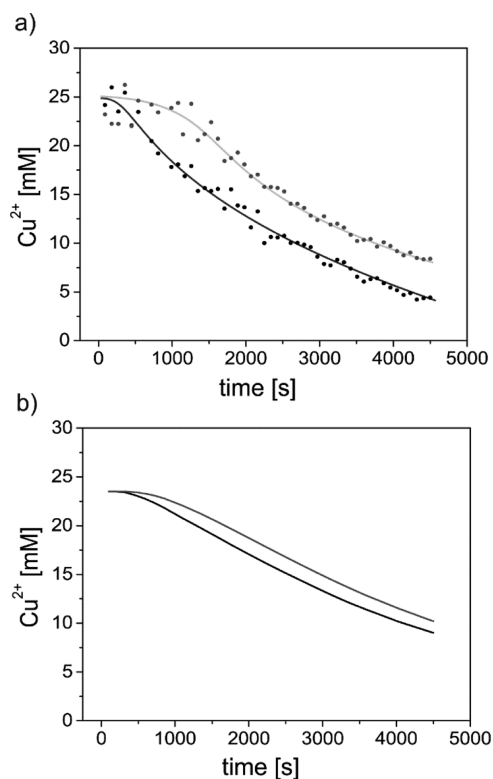

Figure 10. (a) Cu^{2+} concentration variation at $d = 0.313$ mm (black) and 7 mm (gray) along the central axis of the cell for $\Omega = 6.3$ Hz, obtained by MRI and (b) numerical simulations. Lines in (a) are a guide to the eye.

concentrations of Cu^{2+} ions near the rod and in the lower part of the cell have similar values, within the noise level of the experiment. After this time, the concentrations associated with both positions decrease in a rate similar to the concentration curves shown in Figure 3 for $\Omega = 6.3$ Hz. However, for times above 540 s, it is possible to appreciate a decrease in the concentration of Cu^{2+} for $d = 0.313$ mm that is maintained throughout the observation time of the reaction. For times longer than 5000 s, the acquired images show the accumulation of copper on the surface of the Zn disk. As a result, the concentration values obtained for times greater than 4500 s were discarded.

To compare the results, numerical simulations were performed considering a simple surface reaction

$$A_{(aq)} + B_{(s)} \rightarrow P_{(s)} + Q_{(aq)} \tag{8}$$

where A represents Cu^{2+} and Q represents Zn^{2+} ion. The distribution of the species A in the system can be calculated by solving the combined diffusion and convection mass transport differential equation

$$\frac{\partial c}{\partial t} + \nabla \cdot (\vec{u}c) - D\nabla^2 c = 0 \qquad (9)$$

where c and D are the concentration and the diffusion coefficient of A. The fluid velocity ($\vec{u}$) is obtained by numerically solving the Navier−Stokes equation, considering the whole volume of the cell. To solve eq 9, a rapid and complete reaction is assumed. Computational fluid dynamics (CFD) were used to solve the Navier−Stokes equations of flow motion for a RDE cell under convective flow, with similar dimensions and parameters as the used for NMR measurements.

As can be seen, the results obtained by MRI are in agreement with those provided by numerical simulations (Figure 10b). For reaction times below 380 s, both positions show the same concentration value. After this period, the concentration drops in the vicinity of the electrode, whereas in the middle part of the cell, it decays at a slower rate. It is worth to mention that the decay rates obtained by means of MRI are faster than those from CFD. This may be attributed mainly to the idealized model involved in the numerical simulation and, in a lesser extent, to the fact that MRI data are an average over a voxel size (0.313 mm × 0.625 mm × 3 mm), whereas CFD provides data corresponding to a single point. The effect of the magnetic field over the reaction is another factor that the numerical simulation is not taking into account, but it has been reported that is not dominant over the main mass transport process, which in this case is mainly governed by the flow velocities in the cell.[46]

CONCLUSIONS

In this paper, we have explored the possibility of monitoring a chemical reaction in situ under forced hydrodynamic conditions by NMR and MRI. In first place, the artifacts generated in images by NMR due to the presence of metallic objects were studied. It was observed that the presence of a metallic disk with its normal parallel to the static field, B_0 and perpendicular to the radiofrequency field B_1, does not generate appreciable distortions in the images acquired using a spin echo sequence. The copper cementation in an RDE configuration was characterized for different frequencies of rotation, and the rate of the reaction is affected by the flow pattern. Finally, the reaction process was visualized by MRI, acquiring 2D images to obtain maps of Cu^{2+} ions concentration as the reaction developed.

It is shown that the reaction occurs in a localized manner in the regions near the Zn disk, in agreement with the behavior observed in numerical simulations. The pulse sequence used for the experiments is fast enough to capture the moment in which the concentrations associated with the regions near the electrode and the rest of the volume of the solution diverge from each other. However, it may not be fast enough for faster processes or for higher rotation speeds. In the future, this issue could be addressed using a fast sequence of images such as the RARE sequence along with the implementation of the compressed sensing method. It will allow the reconstruction of quantitative concentration maps from sub-sampled images, as was recently demonstrated.[47,48]

MATERIALS AND METHODS

All experiments were carried out at 7.05 T (ν_0 = 300.13 MHz for ^{1}H) in a vertical Oxford superconducting magnet operated with a Kea2 (Magritek GmbH) console. A 3D gradient coil system (Bruker GmbH) with maximum gradients of $1.5 T/m$ was used. Radiofrequency excitation and detection were carried out with a 25 mm inner diameter Bruker GmbH birdcage coil with a length of 37 mm with radiofrequency power driven by a 100 W Tomco amplifier. The system schematized in Figure 1a was built from acrylic and used in all of the experiments. The exterior cylinder with internal radius R_2 = 7 mm is static, whereas the inner cylinder with radius R_1 = 3 mm can rotate. A Zn disc with the same radius is placed in the bottom of this rod. The height of the cell was H_1 = 10 mm and H_2 = 14 mm.

All of the pulse programs and MRI data processing were made using Magritek Prospa software. T_1 relaxation times were measured using the saturation recovery sequence described in Figure S2. For these experiments, 32 points logarithmically spaced were acquired and sequence parameters were set to: τ^* = 100 ms, 90° pulse duration = 300 μs, and a repetition time of 300 ms. T_1 and Cu^{2+} concentration maps were acquired employing the pulse sequence depicted in Figure S2, where a 3 mm slice along the x direction was excited. The field of view was set to 40 mm × 20 mm and matrices of 128 × 32 points were collected, resulting in a spatial resolution of 0.313 mm × 0.625 mm × 3 mm. For all imaging experiments, four signal acquisitions were collected and averaged. The most relevant parameters of the pulse sequence (Figure S3) were the following: echo time t_E = 8 ms, τ^* = 100 μs, τ = 240 μs, hard 90° and 180° pulse duration p_1 = 250 μs, and soft 90° pulse duration of p_2 = 700 μs. Velocity maps were performed using the sequence presented in Figure S1, where velocity-encoded gradients were applied for a time δ = 1 ms, separated by a time delay Δ = 2.2 ms.

Numerical simulations were performed using the finite element method as implemented in COMSOL Multiphysics. The simulations were carried out in a 2D model representing a 3D system with cylindrical symmetry. The geometry of the cell matched the experimental cell geometry. Two coupled processes were incorporated in the simulations: on the one hand fluid dynamics, and on the other hand mass transport and chemical reaction. In a first stage, a time-dependent CFD simulation is carried out in order to obtain the fluid velocity field, $\vec{u}$. This is accomplished by solving the continuity and Navier−Stokes equations for an incompressible, isothermal flow at low Mach number. Viscosity and density parameters corresponding to pure water were used unless otherwise mentioned. In this CFD model, the flow is laminar. No-slip boundary conditions are imposed at the boundaries corresponding to the cell walls and bottom. Rotational boundary conditions are considered at the bottom of the rod and at the shaft of the inner cylinder. In a second stage, mass transport for Cu^{2+} is solved by taking into account diffusion and convection. In order to emulate a mass transport limited reaction, $C_{Cu^{2+}}$ was fixed at 0 at the bottom of the rod. Further details about the model can be found in the Supporting Information.

■ ASSOCIATED CONTENT

Ⓢ Supporting Information

The Supporting Information is available free of charge on the ACS Publications website at DOI: 10.1021/acsomega.8b02460.

> MRI principle, MRI velocity maps, relaxation weighted MRI, and numerical simulations (PDF)

■ AUTHOR INFORMATION

Corresponding Author

*E-mail: racosta@famaf.unc.edu.ar (R.H.A.).

ORCID ⓘ

Manuel Isaac Velasco: 0000-0003-1500-4672
Rodolfo Hector Acosta: 0000-0003-3945-8273

Notes

The authors declare no competing financial interest.

■ ACKNOWLEDGMENTS

■ REFERENCES

(1) *NMR Imaging in Chemical Engineering*; Stapf, S.; Han, S.-I., Eds.; Wiley-VCH, 2006.

(2) Britton, M. M. MRI of Chemical Reactions and Processes. *Prog. Nucl. Magn. Reson. Spectrosc.* **2017**, *101*, 51−70.

(3) Gladden, L. F.; Sederman, A. J. Magnetic Resonance Imaging and Velocity Mapping in Chemical Engineering Applications. *Annu. Rev. Chem. Biomol. Eng.* **2017**, *8*, 227−247.

(4) Klett, M.; Giesecke, M.; Nyman, A.; Hallberg, F.; Lindström, R. W.; Lindbergh, G.; Furó, I. Quantifying Mass Transport during Polarization in a Li Ion Battery Electrolyte by in Situ 7Li NMR Imaging. *J. Am. Chem. Soc.* **2012**, *134*, 14654−14657.

(5) Britton, M. M.; Bayley, P. M.; Howlett, P. C.; Davenport, A. J.; Forsyth, M. In Situ, Real-Time Visualization of Electrochemistry Using Magnetic Resonance Imaging. *J. Phys. Chem. Lett.* **2013**, *4*, 3019−3023.

(6) Gomes, B. F.; Nunes, L. M. S.; Lobo, C. M. S.; Carvalho, A. S.; Cabeça, L. F.; Colnago, L. A. In Situ Analysis of Copper Electrodeposition Reaction Using Unilateral NMR Sensor. *J. Magn. Reson.* **2015**, *261*, 83−86.

(7) Krachkovskiy, S. A.; Bazak, J. D.; Werhun, P.; Balcom, B. J.; Halalay, I. C.; Goward, G. R. Visualization of Steady-State Ionic Concentration Profiles Formed in Electrolytes during Li-Ion Battery Operation and Determination of Mass-Transport Properties by in Situ Magnetic Resonance Imaging. *J. Am. Chem. Soc.* **2016**, *138*, 7992−7999.

(8) Britton, M. M. Magnetic Resonance Imaging of Electrochemical Cells Containing Bulk Metal. *ChemPhysChem* **2014**, *15*, 1731−1736.

(9) Hargreaves, B. A.; Worters, P. W.; Pauly, K. B.; Pauly, J. M.; Koch, K. M.; Gold, G. E. Metal-Induced Artifacts in MRI. *Am. J. Roentgenol.* **2011**, *197*, 547−555.

(10) Lu, W.; Pauly, K. B.; Gold, G. E.; Pauly, J. M.; Hargreaves, B. A. SEMAC: Slice Encoding for Metal Artifact Correction in MRI. *Magn. Reson. Med.* **2009**, *62*, 66−76.

(11) Stradiotti, P.; Curti, A.; Castellazzi, G.; Zerbi, A. Metal-Related Artifacts in Instrumented Spine. Techniques for Reducing Artifacts in CT and MRI: State of the Art. *Eur. Spine J.* **2009**, *18*, 102−108.

(12) Hennig, J.; Nauerth, A.; Friedburg, H. RARE Imaging: A Fast Imaging Method for Clinical MR. *Magn. Reson. Med.* **1986**, *3*, 823−833.

(13) Mansfield, P. Multi-Planar Image Formation Using NMR Spin Echoes. *J. Phys. C: Solid State Phys.* **1977**, *10*, L55.

(14) Bray, J. M.; Davenport, A. J.; Ryder, K. S.; Britton, M. M. Quantitative, In Situ Visualization of Metal-Ion Dissolution and Transport Using1H Magnetic Resonance Imaging. *Angew. Chem., Int. Ed.* **2016**, *55*, 9394−9397.

(15) Carpinella, M.; Velasco, M. I.; Silletta, E. V.; Ovejero, J. M.; Dassie, S. A.; Acosta, R. H. Determination of Flow Patterns in a Rotating Disk Electrode Configuration by MRI. *J. Electroanal. Chem.* **2015**, *750*, 100−106.

(16) Serial, M. R.; Velasco, M. I.; Silletta, E. V.; Zanotto, F. M.; Dassie, S. A.; Acosta, R. H. Flow-Pattern Characterization of Biphasic Electrochemical Cells by Magnetic Resonance Imaging under Forced Hydrodynamic Conditions. *ChemPhysChem* **2017**, *18*, 3469−3477.

(17) Mercado, F. V.; Ovejero, J. M.; Zanotto, F. M.; Serial, M. R.; Velasco, M. I.; Fernández, R. A.; Acosta, R. H.; Dassie, S. A. Facilitated Proton Transfer across Liquid | Liquid Interfaces under Forced Hydrodynamic Conditions. Determination of Partition Coefficients of Neutral Weak Bases. *J. Electroanal. Chem.* **2017**, *791*, 64−74.

(18) Blurton, K. F.; Riddiford, A. C. Shapes of Practical Rotating Disc Electrodes. *J. Electroanal. Chem.* **1965**, *10*, 457−464.

(19) Lord, H. L.; Zhan, W.; Pawliszyn, J. Fundamentals and Applications of Needle Trap Devices: A Critical Review. *Anal. Chim. Acta* **2010**, *677*, 3−18.

(20) Opekar, F.; Beran, P. Rotating Disk Electrodes. *J. Electroanal. Chem. Interfacial Electrochem.* **1976**, *69*, 1−105.

(21) Alexiadis, A.; Cornell, A.; Dudukovic, M. P. Comparison between CFD Calculations of the Flow in a Rotating Disk Cell and the Cochran/Levich Equations. *J. Electroanal. Chem.* **2012**, *669*, 55−66.

(22) Al-Saydeh, S. A.; El-Naas, M. H.; Zaidi, S. J. Copper Removal from Industrial Wastewater: A Comprehensive Review. *J. Ind. Eng. Chem.* **2017**, *56*, 35−44.

(23) Amin, N. K.; El-Ashtoukhy, E.-S. Z. Kinetic Study of Copper Cementation onto Zinc Using a Rotating Packed Bed Cylindrical Reactor. *Can. J. Chem. Eng.* **2010**, *89*, 609−616.

(24) Ekmekyapar, A.; Tanaydin, M.; Demirkiran, N. Investigation of Copper Cementation Kinetics by Rotating Aluminum Disc from the Leach Solutions Containing Copperions. *Physicochem. Probl. Miner. Process.* **2012**, *48*, 355−367.

(25) Zaghib, K.; Chainet, E.; Nguyen, B. Electrochemical Cementation of Copper onto Zinc Kinetics Modifications. *J. Electrochem. Soc.* **1997**, *144*, 3772−3776.

(26) Hargreaves, B. A.; Worters, P. W.; Pauly, K. B.; Pauly, J. M.; Koch, K. M.; Gold, G. E. Metal-Induced Artifacts in MRI. *Am. J. Roentgenol.* **2011**, *197*, 547−555.

(27) Romanenko, K.; Forsyth, M.; O'Dell, L. A. New Opportunities for Quantitative and Time Efficient 3D MRI of Liquid and Solid Electrochemical Cell Components: Sectoral Fast Spin Echo and SPRITE. *J. Magn. Reson.* **2014**, *248*, 96−104.

(28) Blümich, B.; Singh, K. Desktop NMR and Its Applications From Materials Science To Organic Chemistry. *Angew. Chem., Int. Ed.* **2017**, *57*, 6996−7010.

(29) Dalitz, F.; Cudaj, M.; Maiwald, M.; Guthausen, G. Process and Reaction Monitoring by Low-Field NMR Spectroscopy. *Prog. Nucl. Magn. Reson. Spectrosc.* **2012**, *60*, 52−70.

(30) Herrera, A.; Fernández-Valle, E.; Martínez-Álvarez, R.; Molero-Vílchez, D.; Pardo-Botero, Z. D.; Sáez-Barajas, E. Monitoring Organic Reactions by UF-NMR Spectroscopy. *Magn. Reson. Chem.* **2015**, *53*, 952−970.

(31) Reeve, Z. E. M.; Franko, C. J.; Harris, K. J.; Yadegari, H.; Sun, X.; Goward, G. R. Detection of Electrochemical Reaction Products from the Sodium−Oxygen Cell with Solid-State 23 Na NMR Spectroscopy. *J. Am. Chem. Soc.* **2017**, *139*, 595−598.

(32) Boisseau, R.; Bussy, U.; Giraudeau, P.; Boujtita, M. In Situ Ultrafast 2D NMR Spectroelectrochemistry for Real-Time Monitoring of Redox Reactions. *Anal. Chem.* **2014**, *87*, 372−375.

(33) Marino, C.; Dupré, N.; Villevieille, C. Elucidation of Reaction Mechanisms of Ni 2 SnP in Li-Ion and Na-Ion Systems. *J. Power Sources* **2017**, *365*, 339−347.

(34) Bloembergen, N.; Purcell, E. M.; Pound, R. V. Relaxation Effects in Nuclear Magnetic Resonance Absorption. *Phys. Rev.* **1948**, *73*, 679−712.

(35) Power, G.; Ritchie, I. A Contribution to the Theory of Cementation (Metal Displacement) Reactions. *Aust. J. Chem.* **1976**, *29*, 699.

(36) Ku, Y.; Chen, C. H. Kinetic Study of Copper Deposition on Iron by Cementation Reaction. *Sep. Sci. Technol.* **1992**, *27*, 1259−1275.

(37) Demirkiran, N.; Ekmekyapar, A.; Künkül, A.; Baysar, A. A Kinetic Study of Copper Cementation with Zinc in Aqueous Solutions. *Int. J. Miner. Process.* **2007**, *82*, 80−85.

(38) Gros, F.; Baup, S.; Aurousseau, M. Copper Cementation on Zinc and Iron Mixtures: Part 1: Results on Rotating Disc Electrode. *Hydrometallurgy* **2011**, *106*, 119−126.

(39) Dönmez, B.; Sevim, F.; Saraç, H. Kinetic Study of the Cementation of Copper from Sulphate Solutions onto a Rotating Aluminum Disc. *Hydrometallurgy* **1999**, *53*, 145−154.

(40) Bagotsky, V. S. *Fundamentals of Electrochemistry*; John Wiley & Sons, Inc.: Hoboken, NJ, USA, 2005.

(41) Levich, V. G. *Physicochemical Hydrodynamics*; Prentice-Hall: Englewood Cliffs, NJ, USA, 1962.

(42) Cochran, W. G.; Goldstein, S. The Flow Due to a Rotating Disc. *Math. Proc. Cambridge Philos. Soc.* **1934**, *30*, 365−375.

(43) Annamalai, V.; Murr, L. E. Influence of Deposit Morphology on the Kinetics of Copper Cementation on Pure Iron. *Hydrometallurgy* **1979**, *4*, 57−82.

(44) El-Batouti, M. Removal of Copper Metal by Cementation Using a Rotating Iron Cylinder. *J. Colloid Interface Sci.* **2005**, *283*, 123−129.

(45) Vahdat, N.; Newman, J. Corrosion of an Iron Rotating Disk. *J. Electrochem. Soc.* **1973**, *120*, 1682.

(46) Fadali, O. A.; Obaid, M.; Mahmoud, M. S.; Farrag, T. E.; TaeWoo, K.; Khalil, K. A.; Barakat, N. A. M. Copper Ion Cementation in Presence of a Magnetic Field. *Chem. Eng. Technol.* **2015**, *38*, 441−445.

(47) von Harbou, E.; Fabich, H. T.; Benning, M.; Tayler, A. B.; Sederman, A. J.; Gladden, L. F.; Holland, D. J. Quantitative Mapping of Chemical Compositions with MRI Using Compressed Sensing. *J. Magn. Reson.* **2015**, *261*, 27−37.

(48) Gladden, L. F.; Sederman, A. J. Recent Advances in Flow MRI. *J. Magn. Reson.* **2013**, *229*, 2−11.